AIAA SciTech Forum
23-27 January 2023, National Harbor, MD & Online
AIAA SCITECH 2023 Forum

10.2514/6.2023-0634

Optimized Timing Schemes for Multi-Pulse Shake-the-Box Particle Tracking Velocimetry

Michael R. Fenelon,* Yang Zhang,† and Louis N. Cattafesta III‡
Mechanical, Materials, and Aerospace Engineering, Illinois Institute of Technology, Chicago, IL 60616, USA

Nick Morse§
Aerospace Engineering & Mechanics, University of Minnesota, Minneapolis, MN 55455, USA

Krishnan Mahesh¶
Naval Architecture and Marine Engineering, University of Michigan, Ann Arbor, MI 48109, USA

Lanyu Li‖ and Zhao Pan**
Mechanical and Mechatronics Engineering, University of Waterloo, Waterloo, ON N2L3G1, Canada

Particle Tracking Velocimetry (PTV) is a non-intrusive measurement technique that is gaining increasing popularity in the experimental fluid mechanics community. The basic working principle is to determine three-dimensional Lagrangian particle tracks via multiple exposures separated by known time intervals as seen by at least three cameras. The practical extension of PTV to three-dimensional tracks was enabled by the introduction of the *Shake-the-Box* algorithm, which can accurately determine three-dimensional particle trajectories. However, the selected timing strategy of the multi-pulse (i.e., four in this paper) technique is not clearly defined *a priori*. The accuracy of the reconstructed pathline depends on the timing strategy of the four pulses and the selected temporal interpolation/fitting methods. By examining several canonical flows, this study aims to investigate the dt timing strategy, whether the pulses should be symmetric or asymmetric with respect to the midpoint of the two middle pulses, and to assess the uncertainty from different pathline reconstruction methods, i.e., quadratic and cubic polynomial fitting and Radial Basis Functions (RBF). The results indicate that a symmetric timing scheme is consistently better than an asymmetric timing scheme for a fixed total track duration, and that RBF-based fitting is slightly better than polynomial fits because it provides a good compromise between accuracy and error assessment. The error scaling associated with the timing schemes is also quantified.

I. Introduction and motivation

Prior to Elsinga's study on how to implement three-dimensional (3D) Tomographic Particle Image Velocimetry (TOMO-PIV), the main ways of conducting PIV experiments were mainly 2-component and 3-component planar PIV [1]. Two-component planar PIV allows for two orthogonal in-plane velocity components of the flow to be resolved. A version from [2] called stereo-PIV, allowed for the third (out-of-plane) component of velocity to be resolved [2] with the use of a second camera. However, in order to fully quantify and characterize complex flow phenomena, such as turbulent flow structures, all velocity components have to be measured in a volume.

One way to capture the 3D flow behavior of flow fields is TOMO-PIV. This technique involves at least 3 cameras acquiring particle images from different perspective views to resolve the 3 components of the flow velocity in a volume. However, a 4-camera configuration has proven to be the de facto standard in such experiments [1]. While TOMO-PIV is widely used in quantifying 3D velocity fields, it falls short of particle tracking. With the introduction of fluid

*Graduate Research Assistant, AIAA Student Member.
†Research Assistant Professor, AIAA Member,
‡Olin Endowed Chair and Professor, AIAA Fellow.
§Graduate Research Assistant.
¶Professor, AIAA Associate Fellow.
‖Graduate Research Assistant.
**Assistant Professor.

trajectory correlation (FTC) [3], motion tracking enhanced (MTE), and sequential motion tracking enhanced (SMTE) [4], TOMO-PIV has arguably migrated towards particle tracking. Progressing from these two previous techniques, MTE and SMTE, a new method, *Shake-the-Box* (STB), was introduced, which allowed for accurate determination of particle trajectories with seeding densities approaching that of TOMO-PIV [5].

The working principle of STB consists of identifying particles via iterative particle reconstruction (IPR) [6], using TOMO-PIV as a way to predict the general direction of the flow, and then the *'shaking'* step, where the particles are placed in different positions within a certain search radius (generally less than 1 pixel) and evaluated against residual images for accurate particle placement [5]. This method/algorithm can be used to construct n-length particle tracks (n being the number of particle images). A feature in an $n = 4$ pulse algorithm is that a cubic polynomial can be used to represent the Lagrangian particle trajectory, which allows for calculating a time-varying acceleration. The limitations in the accuracy of this technique are similar to TOMO-PIV: calibration, image pre-processing, volume reconstruction, etc. However, a main limitation in STB is the amount of time (dt) between each particle image pair. If the dt between each particle image pair is too small, or the particular regional velocity is too low, it will result in major particle overlap, and STB cannot distinguish the particle between the images [7]. On the other hand, if the dt is too large, the longer track duration will lead to increasing tracking error. Therefore, for both total track yield and acceptable uncertainty, proper selection of the dt is needed [7, 8].

A particular subset of STB is multi-pulse (MP)-STB where double-exposed, dual-frame PIV cameras are used to determine particle trajectories. The MP-STB technique is similar to STB, but the main difference is in the variable time separation between each particle image pairs. For a typical MP-STB system using two double-pulse Nd:YAG lasers, four particle images are taken, separated by three dt. These dt can vary and $dt1$ need not be identical to $dt3$; their value will depend on the type of flow being examined [7]. Using MP-STB with a flow measurement software, e.g., LaVision DaVis, the general tracking scheme is as follows and illustrated in Figure 1.

1) Capture four particle images separated by three dt.
2) Perform a cross-correlation between the second and third particle images to locate the particles.
3) Extrapolate using the velocity from the previous step to estimate the 1st and 4th particle locations.
4) Iteratively 'shake' the first and fourth particles to accurately find their locations.
5) Fit a polynomial (2^{nd} or 3^{rd} order) to the 4-particle track.

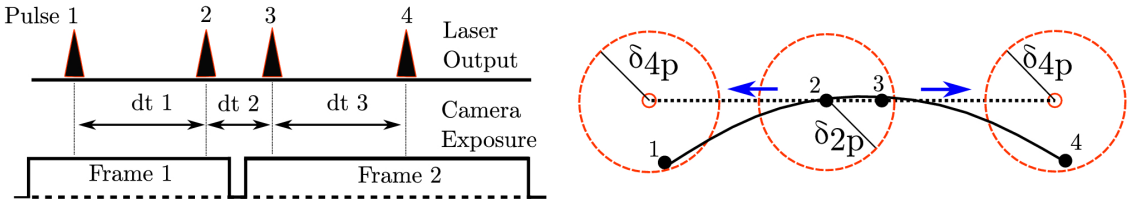

Fig. 1 Example MP-STB particle tracking and pathline reconstruction [9].

MP-STB excels when dealing with high speed subsonic flows (> 40 m/s), where the hardware is limited in the number of images it can acquire, thereby limiting the track length [7]. The light source (typically two double-pulse lasers) timing strategy seeks to select the optimal dt. Since the tracks have a length spanning 4 particle positions, there are three dt that have to be set to separate each pulse. This leads to an expression for the track duration T as the sum of the three dt

$$T = dt1 + dt2 + dt3 \tag{1}$$

Since the middle dt ($dt2$) is determined by standard PIV considerations, it can be used as a time scale for nondimensionalizing the equation, which allows for studying the effects of changing the size of $dt1$ and $dt3$. Note that $dt1^*$ equals $dt3^*$ for symmetric timing schemes.

$$\frac{T}{dt2} = \frac{dt1}{dt2} + 1 + \frac{dt3}{dt2} \tag{2}$$

$$T^* = dt1^* + 1 + dt3^* \tag{3}$$

Studies that have utilized this technique, but have used a generally accepted long-short-long timing strategy, include boundary layer flow investigation [7], higher speed flows over a curved geometry [10], and flow over a laminar wing

[11]. This study aims to investigate the effects of the timing strategy based on the type of flow being examined, such as oscillatory flow, rotational flow, and turbulent flow, etc. Then, the optimization of the timing strategy is obtained from this study.

II. Methodologies

To assess the timing strategy and pathline reconstruction methods, 'ground truth' answers are needed. Therefore, three exact solutions are used for assessment: Stokes's oscillating plate, a synthetic jet DNS, and a turbulent channel flow DNS. Three different pathline fitting methods: 2^{nd} and 3^{rd} order polynomials, and radial basis function (RBF)-based fits, are used and compared to evaluate the errors by comparing the computed tracks with the 'ground truth'. The error associated with each pathline fitting method will be evaluated in each flow case.

A. Polynomial Fitting

The first fitting method is the 2^{nd} order polynomial:

$$\boldsymbol{x}(t) = \frac{At^2}{2} + Bt + C \tag{4}$$

$$\dot{\boldsymbol{x}}(t) = At + B \tag{5}$$

$$\ddot{\boldsymbol{x}}(t) = A \tag{6}$$

The second temporal derivative of the 2^{nd} order polynomial is a constant in Equation 6, which indicates a constant acceleration. For a given pathline, a constant acceleration may not be accurate, especially when considering pathlines of highly unsteady flows. The next fitting method is the 3^{rd} order polynomial:

$$\boldsymbol{x}(t) = \frac{At^3}{3} + \frac{Bt^2}{2} + Ct + D \tag{7}$$

$$\dot{\boldsymbol{x}}(t) = At^2 + Bt + C \tag{8}$$

$$\ddot{\boldsymbol{x}}(t) = 2At + B \tag{9}$$

The second temporal derivative of the 3^{rd} order polynomial is time dependent in Equation 9, meaning a time dependent acceleration, which likely provides a more accurate representation of the acceleration for a given pathline.

Apart from the acceleration, quantifying the error associated with the fitting methods is also critical. For each of these fitting methods, the computed pathline uses 4 points from the MP-STB data. For a 2^{nd} order polynomial, the computed pathline does not pass through all 4 points, which means that a regression error can be used to estimate the uncertainty. However, for the 3^{rd} order polynomial, the computed pathline passes through all 4 points exactly, which means the uncertainty cannot be quantified via a regression error.

B. RBF-QR

RBF is a meshless algorithm. It uses the Euclidean norm as an independent variable to approximate scattered data. It can have infinite smoothness and be extended to higher dimensions (2 or 3 dimensions in the current study). In the domain, the particle positions $\boldsymbol{x}_i^c \in \mathbb{R}$ are given at N scattered snapshot time $t_i^c \in \mathbb{R}$, where $i = 1, 2, \ldots, N$ ($N = 4$ in the current study). The classic RBF, also known as the RBF-Direct in some literature [12–14], has its approximation function $\tilde{x}(t)$:

$$\tilde{x}(t) = \sum_{i=1}^{N} \lambda_i \phi(\epsilon, \left\|t - t_i^c\right\|) = \boldsymbol{\Phi}\boldsymbol{\Lambda}, \tag{10}$$

where $\phi(\epsilon, \left\|t - t_i^c\right\|)$ is an RBF kernel such as the Gaussian kernel $\phi = \exp(-\epsilon^2 \left\|t - t_i^c\right\|^2)$ with $\boldsymbol{\Phi}$ being the matrix form, ϵ is the shape factor that controls the flatness of radial basis, λ_i is the expansion coefficient that controls the weight of

basis functions with $\mathbf{\Lambda}$ being the matrix form. The expansion coefficient λ_i can be calculated by forcing $\tilde{x} = x_j^c$ when $t = t_j^c$: $\tilde{x}(t_j^c) = \sum_{j=1}^{N} \lambda_i \phi(\epsilon, \left\| t_j^c - t_i^c \right\|),\ i, j = 1, 2, ...N$.

However, the shape factor ϵ needs to be carefully chosen to provide both an accurate approximation to the function and well-conditioning of a matrix system in the RBF-Direct. A small ϵ, corresponding to the flat radial basis, can potentially have high-accuracy approximation; however, it often leads to an ill-conditioned matrix. On the contrary, a large ϵ, corresponding to a sharp radial basis, has a well-conditioned matrix but often leads to inaccurate approximation results. The relations between the Gaussian RBF-Direct kernel and the shape factor are shown in Figure 2. To balance these deficiencies, a stable RBF algorithm, i.e., the RBF-QR is adapted. The RBF-QR converts the RBF-Direct basis Φ to a stable RBF-QR basis Ψ, which permits small shape factors. More details about the RBF-QR can be found in [12, 13].

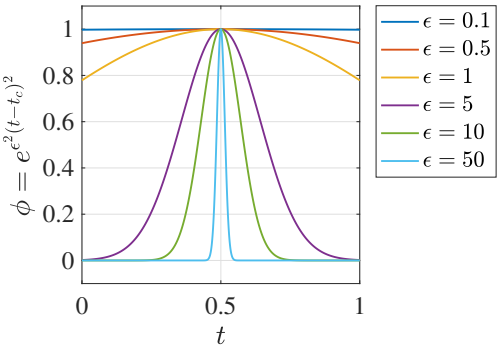

Fig. 2 Gaussian RBF-Direct kernel with different shape factor ϵ.

Similar to polynomial fitting, the reconstructed pathline from RBF can either go through all particle locations (like the 3^{rd} order polynomial fitting) or closely pass by all particle locations with a least square fitting error (like the 2^{nd} order polynomial fitting). In the case of an analytical solution without added noise, the pathlines are supposed to go through all particle locations. On the other hand, with added noise or measurement error associated with experimental data, the pathlines are not required to go through all particle locations since there are uncertainties associated with the particle locations. To impose the least squares algorithm, we first reconstruct the RBF-QR system matrix $\mathbf{\Psi}$ using M reference snapshot time $\boldsymbol{t}^{\text{ref}}$ along tracks and N measured snapshot time $\boldsymbol{t}^c$. The system matrix $\mathbf{\Psi}$ has the entries: $\Psi_{ij} = \psi\left(\epsilon, \left\| \boldsymbol{t}_i^c - \boldsymbol{t}_j^{\text{ref}} \right\|\right)$, where $i = 1, 2, ..., N,\ j = 1, 2, ..., M$. The ratio of the number of the snapshots between the given snapshot time and the reference snapshot time is the over-sampling ratio $\beta = N/M$ [15]. $\beta > 1$ is required to formulate an over-determined mapping to fit data, instead of interpolation. The evaluation matrix $\mathbf{E}$ is formulated to map between N_{eval} evaluation snapshot time $\boldsymbol{t}^{\text{eval}}$ and reference snapshot time $\boldsymbol{t}^{\text{ref}}$: $E_{kj} = \psi\left(\epsilon, \left\| \boldsymbol{t}_k^{\text{eval}} - \boldsymbol{t}_j^{\text{ref}} \right\|\right)$, where $j = 1, 2, ..., M,\ k = 1, 2, ..., N_{\text{eval}}$. Then we are able to establish the least squares RBF-QR approximation in x direction as:

$$\tilde{x}(t) = \mathbf{E}\mathbf{\Psi}^{+}\boldsymbol{x}^c. \tag{11}$$

Invoking that the system matrix $\mathbf{\Psi}$ is non-square, generalized inverse $\mathbf{\Psi}^{+} = (\mathbf{\Psi}^T\mathbf{\Psi})^{-1}\mathbf{\Psi}^T$ is needed to solve the least squares problem.

For the velocity and acceleration evaluation, the RBF-QR system matrix $\mathbf{\Psi}$ remains unchanged but the evaluation matrix becomes $\mathbf{E}_t = \frac{d\mathbf{E}}{dt}$ and $\mathbf{E}_{tt} = \frac{d^2\mathbf{E}}{dt^2}$, respectively. The velocity and acceleration functions reconstructed by the RBF-QR have infinite smoothness. More details about the RBF-QR differentiation can be found in [13, 15].

C. Stokes's Oscillating Plate

Starting with Stokes's oscillating plate, there is an analytical solution for this 2D flow field:

$$u\,(y,t) = U_0\,\exp\left(-\sqrt{\frac{\Omega}{2\nu}}y\right)\cos\left(\Omega t - \sqrt{\frac{\Omega}{2\nu}}y\right) \tag{12}$$

where $u\,(y,t)$ is the horizontal velocity, y is the vertical distance from the oscillating plate, t is the time elapsed in the simulation in units of seconds, U_0 is the velocity of the plate, Ω is the plate oscillation frequency, and ν is the kinematic viscosity of the fluid (air in the current case).

To provide nondimensional results, the x and y positions can be nondimensionalized by the diffusion length scale $\sqrt{2\nu/\Omega}$. Additionally, the time can be nondimensionalized as Ωt.

$$X = \frac{x}{\sqrt{\frac{2\nu}{\Omega}}} \text{ and } Y = \frac{y}{\sqrt{\frac{2\nu}{\Omega}}} \tag{13}$$

$$\phi = \Omega t \tag{14}$$

The phase-locking timing scheme to mimic an MP-STB measurement is illustrated in Figure 3a, where the phase instance is centered between the second and third pulses. In the current case, 16 equally spaced phases are sampled. As an example, shown in Figure 3b, multiple tracks at different heights Y are shown, where the track closest to the plate (black pathline) is used for error demonstration in this case. From this model, the values of $dt1^*$ and $dt3^*$ can be varied to test the effects of the timing scheme on the error associated with different pathline computation: 2^{nd} order polynomial, 3^{rd} order polynomial, and the RBF-QR.

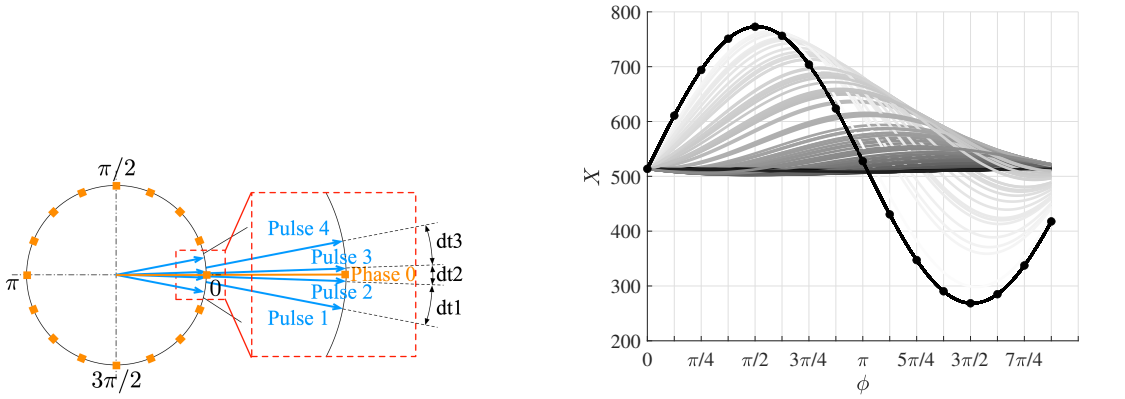

(a) An example of a laser pulse timing scheme

(b) Pathlines of simulated particles at different heights

Fig. 3 Simulated phase-locking measurements of Stokes's oscillating plate pathlines.

D. Synthetic Jet DNS

The second truth source to use for MP-STB simulations is the DNS of a synthetic jet. The DNS is performed using the unstructured numerical method developed by Mahesh et al. [16] for solving the incompressible Navier-Stokes equations using a predictor-corrector formulation. The algorithm emphasizes discrete kinetic energy conservation to ensure robustness without added numerical dissipation, and has been validated for a variety of flows, including regular jets [17] and steady and pulsed transverse jets [18–20]. The DNS is designed to model a physical experiment, in which a synthetic jet (small speaker) is placed in a housing (i.e., cavity). When actuated, the air passes through an orifice smaller than the speaker diameter, which can be seen in Figure 4 with the domain sizing and boundary conditions labeled. The cavity volume and diameter match that of the experimental configuration, where the orifice diameter D is 4.22 mm. The Reynolds number and Stokes number of the DNS are given as

$$Re = \frac{U_{mean} D}{\nu} = 1350, \tag{15}$$

$$S = \sqrt{\frac{\omega D^2}{\nu}} = 26.7, \tag{16}$$

where ω is the frequency of the jet oscillation and the inflow boundary condition is set such that the mean and phase velocity at the jet exit plane are $U_{mean} = 1$ and $U_{phase} = \frac{\pi}{2}\sin(\omega t)$. The computations are performed on a grid of 68

million control volumes partitioned across 1280 processors with 400 grid points distributed around the jet circumference. The solution is advanced 12000 times per jet cycle using Crank-Nicolson implicit time-stepping.

To compute the pathlines of the seeding particles in the DNS, Lagrangian tracer probes are used to collect the position of the particles. In the DNS, the tracer probes are initially seeded randomly in a subdomain around the jet exit and their velocities are controlled by the equations below, where Equation 17 advects the probes and Equation 18 interpolates the velocity of the probes from the adjacent control volume (cv).

$$x_{i,p}^{k} = x_{i,p}^{k-1} + V_{i,p}^{k-1}\Delta t_p \tag{17}$$

$$V_{i,p} = u_{i,cv} + \left(x_{j,p} - x_{j,cv}\right)\left(\frac{\partial u_i}{\partial x_j}\right)_{cv} \tag{18}$$

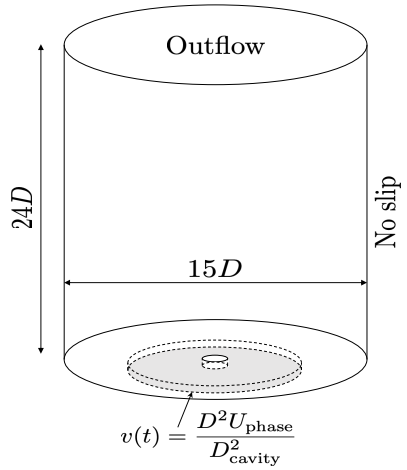

Fig. 4 Synthetic jet DNS schematic

E. Johns Hopkins University turbulent channel flow

Another simulated 3D turbulent flow field tested in the current study is from the Johns Hopkins Turbulence Databases. The Reynolds number and time scale are defined below, where u_τ is the friction velocity, h is the half-channel height, and ν is the viscosity of air.

$$Re_\tau = \frac{u_\tau h}{\nu} = 1000, \tag{19}$$

$$t^* = \frac{t}{\frac{h}{u_\tau}}. \tag{20}$$

The channel flow is produced from DNS of wall bounded channel flow with periodic boundary conditions in the longitudinal and transverse directions, and no-slip conditions at the top and bottom walls. The channel flow has a domian size of $8\pi \times 2 \times 3\pi$, using $2048 \times 512 \times 1536$ nodes. The incompressible N-S equations are solved using the pseudo-spectral (Fourier-Galerkin) method in wall-parallel planes, and the 7th-order B-spline collocation method in the wall-normal direction. More details regarding the simulation are referred to the database [21].

III. Results and Discussions

A. Stokes's Oscillating Plate

To evaluate the error of the reconstructed pathline for different timing schemes, $dt1^*$ and $dt3^*$ are varied from 1 to 6 while $dt2$ is kept constant as $\frac{\pi}{32}$ (seconds). An example is illustrated in Figure 5 for different timing schemes at the

targeted phase $\phi = \frac{3\pi}{8}$, in which the red marker represents the measured phase and four blue markers represent the 4 pulses. Figure 5a shows a short $dt1^*$, while Figure 5b shows a long $dt1^*$ such that the track duration T spans the neighboring phases.

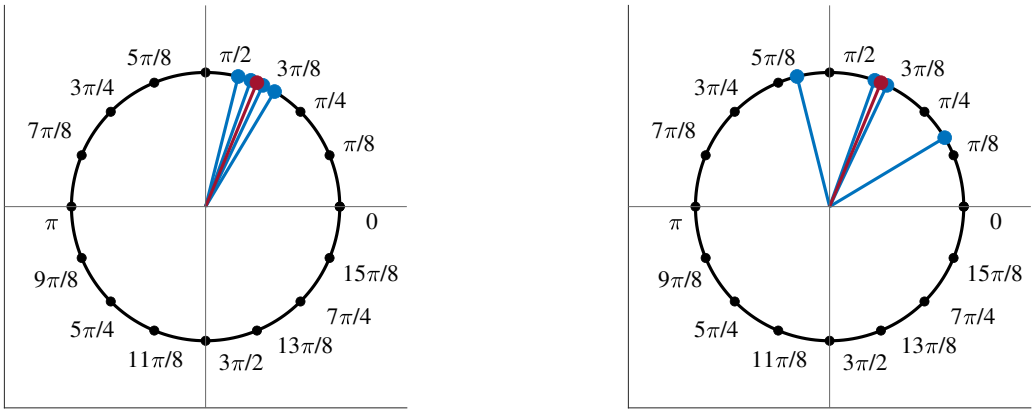

(a) Laser-pulse timing, $dt1^* = dt3^* = 1$ **(b) Laser-pulse timing,** $dt1^* = dt3^* = 6$

Fig. 5 Simulated MP-STB laser-pulse timing

In reference to the unit circle, phase $\phi = \frac{3\pi}{8}$ is used to demonstrate the quantitative fitting error of the computed pathlines compared to the *true* pathlines. Figure 6a provides the comparison of the computed pathlines to the reference pathline, while Figure 6b shows a zoomed in view such that the differences between the reconstructed pathlines and reference pathline (dotted black line) are noticeable. It is clear that the 2^{nd} order polynomial fitting is incorrect, while the other two methods provide a close match.

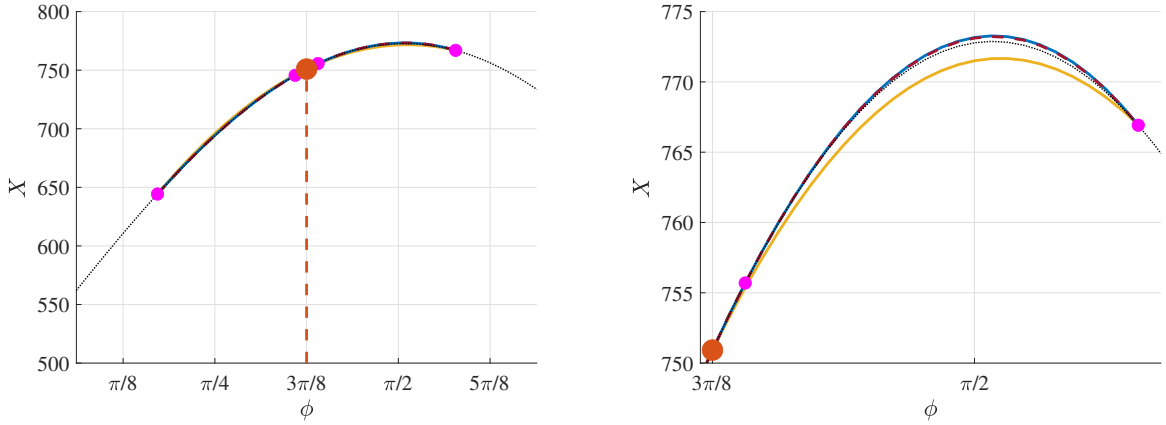

(a) Pathline fitting comparison, $dt1^* = dt3^* = 6$ **(b) Pathline fitting comparison, zoomed in view**

Fig. 6 Pathline fit comparisons at phase $\frac{3\pi}{8}$. Red marker indicates the measured phase, four magenta markers indicate 4 pulse instances. — 2^{nd} order; — 3^{rd} order; - - RBF-QR; ··· analytical solution.

The RMS error and the maximum error of the track fitting are calculated to assess the error. The computation for the RMS error is as follows:

1) Compute the Euclidean error (Δs_i between the computed pathline and the true pathline at discrete time instances (t_i)

$$\Delta s_i = \sqrt{(x_{\text{fit}}(t_i) - x_{\text{true}}(t_i))^2 + (y_{\text{fit}}(t_i) - y_{\text{true}}(t_i))^2 + (z_{\text{fit}}(t_i) - z_{\text{true}}(t_i))^2}, \tag{21}$$

2) Compute the RMS of the Euclidean error (Δs_i) and normalize by the diffusion length scale (this metric is now a

function of the phase angle ϕ)

$$e_{\phi_n} = \frac{RMS\left(\Delta s_i\right)}{\sqrt{\frac{2\nu}{\Omega}}}, \tag{22}$$

3) Compute the RMS of e_{ϕ_n} over all phase angles (this is now the error for individual pathlines)

$$e_p = RMS\left(e_{\phi_n}\right), \tag{23}$$

4) Compute the RMS of e_p over the whole domain (this is now the error for the entire flow domain)

$$e_r = RMS\left(e_p\right). \tag{24}$$

The maximum error is taken as the maximum value of the Euclidean errors for all phases and pathlines, and the calculation is given below:

$$e_{\phi_{n_{max}}} = \frac{\max\left(\Delta s_i\right)}{\sqrt{\frac{2\nu}{\Omega}}} \tag{25}$$

$$e_{p_{max}} = \max\left(e_{\phi_{n_{max}}}\right) \tag{26}$$

$$e_{r_{max}} = \max\left(e_{p_{max}}\right) \tag{27}$$

In the simulated MP-STB measurements, $dt1^*$ and $dt3^*$ are varied independent of each other from 1 to 6, meaning both symmetric and asymmetric timing schemes are considered. The subsequent plots show the results of the RMS and maximum error computations for each type of pathline fitting method. The results are compared in Figures 7 and 8. Note that the color bar range for the 2^{nd} order polynomial fitting is one order magnitude larger than the 3^{rd} order polynomial fitting and RBF-QR in the contour plots. For all three methods, combination of smaller $dt1^*$ and $dt3^*$ results in smaller (both RMS and maximum) errors in the reconstructed pathlines. For a fixed track duration (i.e., $dt1^* + dt3^*$ is a constant), the asymmetric dt scheme appears to be worse than the symmetric timing scheme in this case.

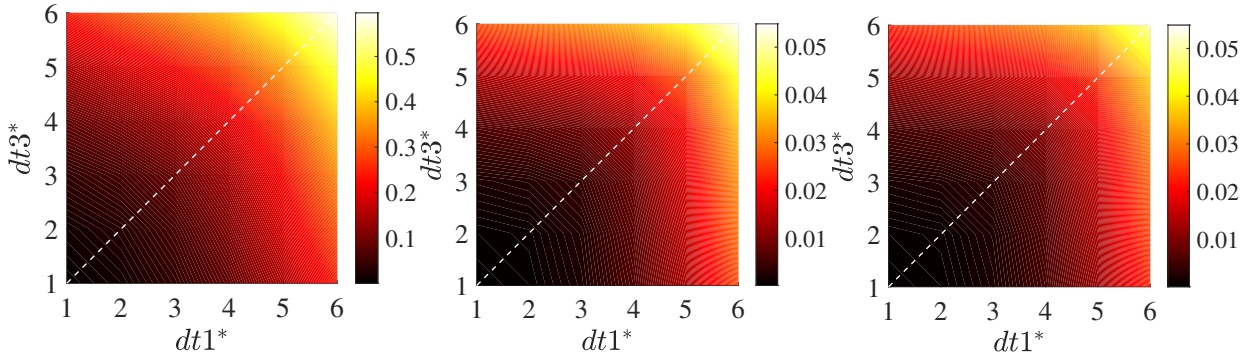

(a) 2^{nd} **order polynomial** **(b)** 3^{rd} **order polynomial** **(c) RBF-QR**

Fig. 7 Contour of e_r for different $dt1^*$ and $dt3^*$ for Stokes's oscillating plate. Dashed line indicates the symmetric timing scheme.

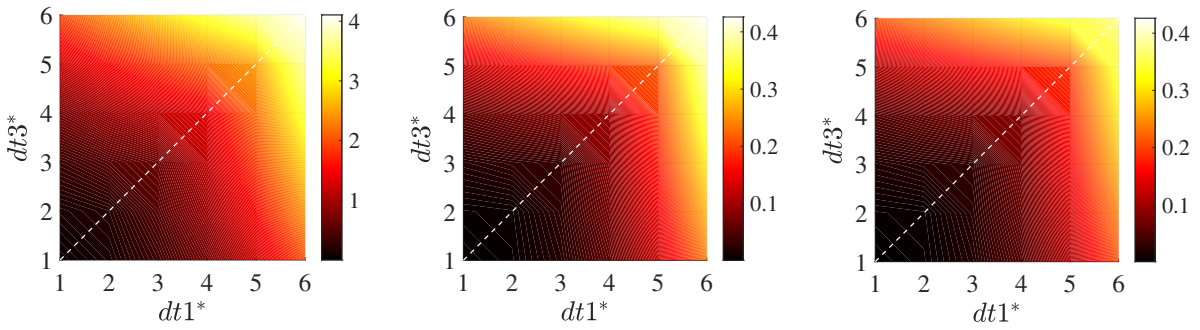

(a) 2^{nd} order polynomial **(b) 3^{rd} order polynomial** **(c) RBF-QR**

Fig. 8 Contour of $e_{r_{max}}$ for different $dt1^*$ and $dt3^*$ for Stokes's oscillating plate. Dashed line indicates the symmetric timing scheme.

In order to obtain a scaling law of the error matrices, the error values from the symmetric timing scheme are extracted. Applying a power law fitting with least-square-error, the error vs. $dt1^*$ for different methods are compared in Figure 9 using logarithmic scales. In Figure 9a, the error of 2^{nd} order polynomial fitting follows a trend of $e_r \approx (dt1^*)^{2.54}$, while the error trends of the other two are approximately $(dt1^*)^{3.42}$. For this type of flow, the maximum errors in Figure 9b all follow very similar trends as in Figure 9a. From the comparisons, it is clear the 2^{nd} order polynomial fitting is worse than the other two, while the other two are comparable.

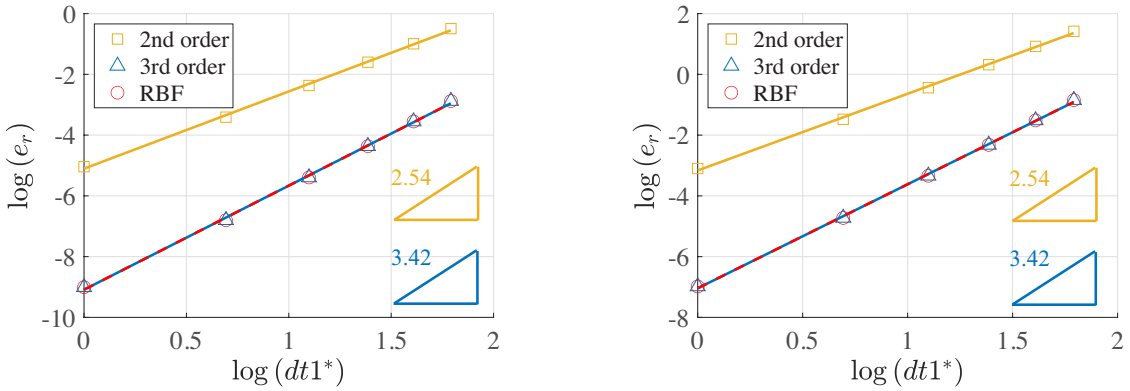

(a) e_r power scaling **(b) $e_{r_{max}}$ power scaling**

Fig. 9 Power scaling relationships for RMS and maximum errors for symmetric timing schemes for the case of Stokes's oscillating plate. The power factors are given in the plots.

B. DNS of a synthetic jet

In the DNS, a total number of 21620 particles are randomly seeded into the simulation domain, see Figure 10a. Only a subset of 2162 particles are used for the MP-STB simulations. For this 3D turbulent case, an example track from DNS is projected in the $x-y$ plane, see Figure 10b, where the orifice diameter D is used as the characteristic length in this study. Unfortunately, the simulation records are only saved to phase $13\pi/8$. Therefore, the records are divided into 14 phases with an increment of $\pi/8$. The jet cycle period is 10 ms. The entire simulation cycle was meant for 12000 snapshots, which is equivalent to a time step between each snapshot of 0.83 μs. For the MP-STB simulations, $dt2$ is set as 25 μs (30 simulation time steps). Therefore, a $dt1^*$ or a $dt3^* = 6$ is equivalent to a 150 μs pulse separation physically. In Figure 10b, the red markers indicate the 14 time instances for the simulated phase-locking measurements along the track.

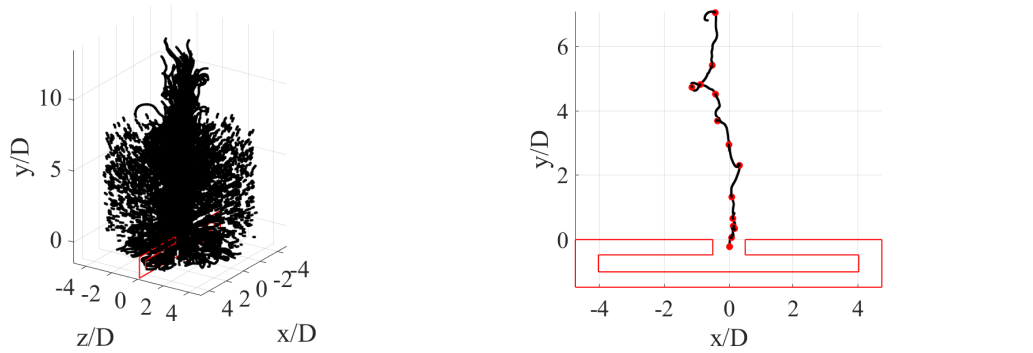

(a) All particle tracks in the domain **(b) Example track with 14 phases along the track**

Fig. 10 Particle tracks in the synthetic jet DNS. The red profile represents the synthetic jet cavity.

To quantify the accuracy of the timing scheme using different fitting methods, the errors are calculated similar to the previous Stokes's oscillating plate (Equations 21 to 24). The errors are first calculated at each phase for each pathline in the domain, then the RMS and maximum errors are calculated. The results of the RMS error and maximum error are given in the Figures 11 and 12. Note that the values along the diagonals are the symmetric timing schemes ($dt1^* = dt3^*$). In the RMS error plots, the contour patterns are almost symmetric about the diagonals. It is clear that the 2^{nd} order polynomial is the worst, while the other two are comparable for symmetric timing schemes. Also, the symmetric timing scheme is better than asymmetric timing schemes for a given track duration for all methods. It is interesting that the 2^{nd} order polynomial fitting can be slightly better than the other two for some asymmetric timing schemes, for example, when $dt1^* = 1, dt3^* = 6$ or $dt1^* = 6, dt3^* = 1$. For the maximum errors, the biggest difference is that the error contour patterns are no longer diagonal symmetric. The 2^{nd} order polynomial is generally worse than the other two. Again, symmetric timing schemes are suggested to obtain a smaller maximum error.

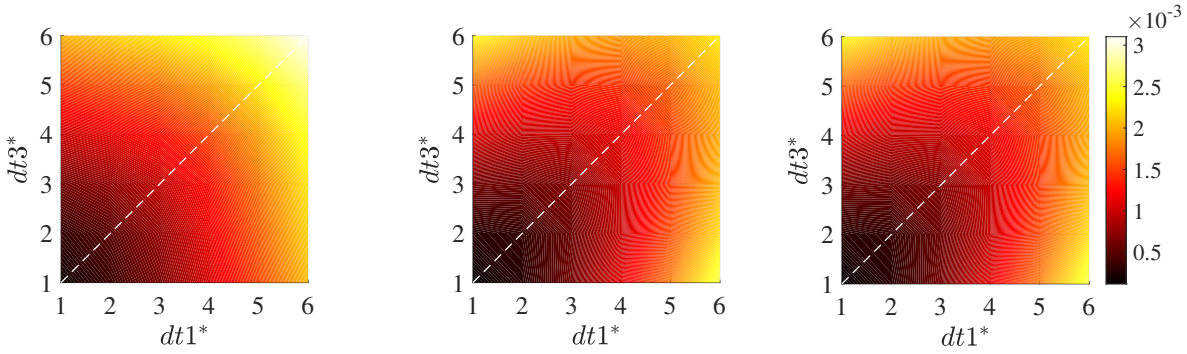

(a) 2^{nd} order polynomial **(b) 3^{rd} order polynomial** **(c) RBF-QR**

Fig. 11 Contour of e_r for different $dt1^*$ and $dt3^*$ combinations for synthetic jet DNS. Dashed line indicates the symmetric timing scheme.

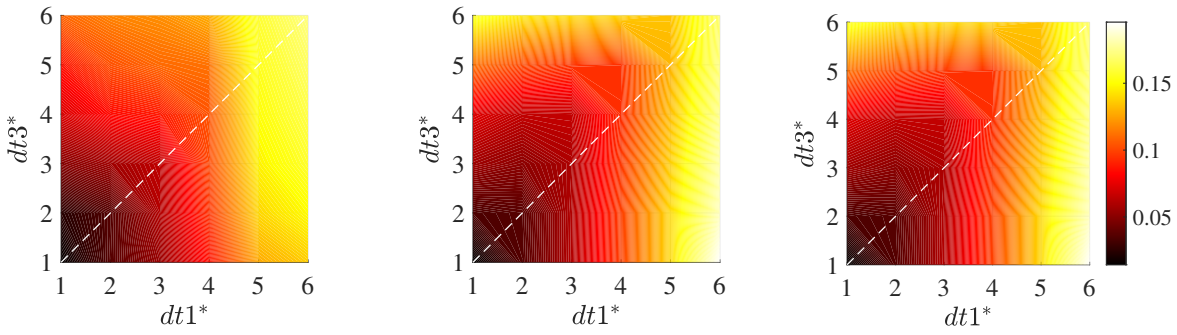

(a) 2^{nd} order polynomial **(b) 3^{rd} order polynomial** **(c) RBF-QR**

Fig. 12 Contour of $e_{r_{max}}$ for different $dt1^*$ and $dt3^*$ combinations for synthetic jet DNS. Dashed line indicates the symmetric timing scheme.

Similar to the previous Stokes's oscillating plate, the errors of the symmetric timing schemes are fitted using power law and are compared in Figure 13. For the RMS error, the error of all three methods nicely follow the power law trend. The 2^{nd} order polynomial has a trend of $e_r \approx (dt1^*)^{1.56}$, while the other two have $e_r \approx (dt1^*)^{1.65}$. Again, the 2^{nd} order polynomial fitting appears to be worse than the other two in Figure 13a. However, for the maximum errors in Figure 13b, all three methods have comparable performance at the small $dt1^*$ initially, and then the 2^{nd} order polynomial fitting becomes worse as $dt1^*$ increases. Therefore, the 2^{nd} order polynomial is only slightly worse than the other two methods considering both the RMS and maximum errors.

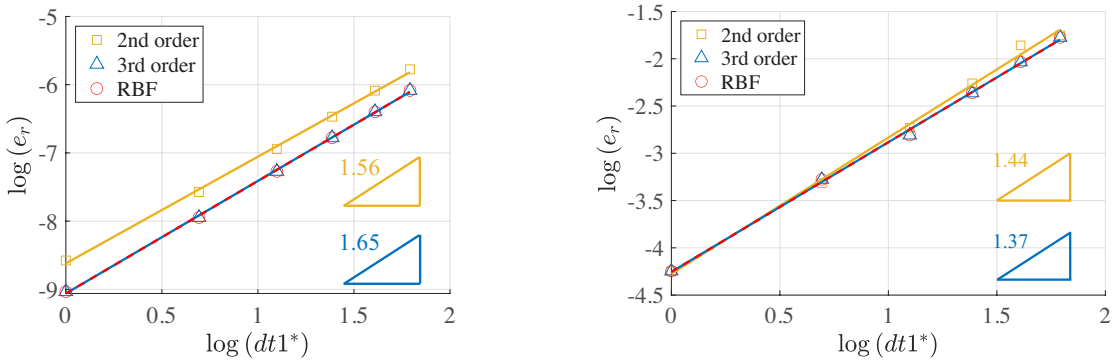

(a) e_r power scaling **(b) $e_{r_{max}}$ power scaling**

Fig. 13 Power scaling relationships for RMS and maximum errors for symmetric timing schemes for synthetic jet DNS. The power factors are given in the plots.

C. Turbulent Channel Flow DNS

Unlike the previous two cases, the stationary channel flow has no periodicity, which means there is no phase locking. Therefore, to systematically sample points along the particle trajectories, particles are sampled at evenly distributed time instances. For example, the nondimensional time domain for the DNS is $t^* = [0, 26]$, and the measurement time instances are percentages of the total time (e.g., $26 \times [0, 0.1, 0.2, ..., 1]$). In this example, the time interval is 10% of the total simulation time. The information before time $t^* = 0$ and after $t^* = 26$ of the simulation is unknown; thus, those points cannot be used. Therefore, 9 targeting times instances are used to perform the MP-STB simulations for each particle track. Figure 14a shows all particle tracks in the domain, while Figure 14b illustrates a single track with the nominal sample times indicated. Note that in the real experiments, a subdomain (the green box) is selected to improve the spatial resolution. In the current study, to obtain converged statistics, a total number of 324 seeding particles in the whole domain from the database are collected in the MP-STB simulations. The particles are distributed across the whole simulation domain, which includes the near wall regions of the channel. Each particle is spatially and temporally interpolated by the JHU DNS database query system for every time interval, i.e., t_i^* to t_{i+1}^*. Again, the combinations

of $dt1^*$ and $dt3^*$ from 1 to 6 are tested. The $dt2$ is kept as 17.2 seconds (twice the simulation dt), where the total dimensional simulation time is about 1700 seconds.

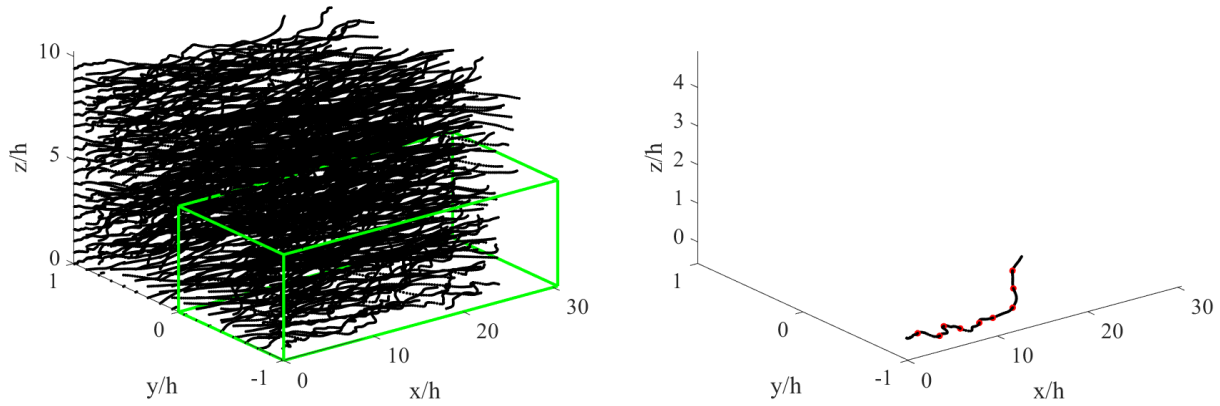

(a) Channel Flow with subregion containing example track (b) Track within subregion (measurement points shown in red)

Fig. 14 Particle tracks in the turbulent channel flow DNS.

To assess the accuracy of the path-fitting methods, the same error computations as in the previous cases are adopted here. First looking at the RMS error contours in Figure 15, as also seen in the cases of Stokes's oscillating plate and synthetic jet DNS, there is a diagonal symmetry shown in the contour plots. Looking more closely at $dt1^* = 1$ and $dt3^* = 6$ or vice versa, the 2^{nd} order polynomial is slightly better than the 3^{rd} order polynomial and the RBF-QR, this may be due to the 3^{rd} order polynomial and RBF-QR over-fitting the tracks. For the maximum error, the 2^{nd} order polynomial appears better for a majority of values for $dt1^*$ and $dt3^*$. This implies that the 3^{rd} and RBF-QR fittings may perform worse (over-fitting) at certain locations using an asymmetric timing scheme. In both RMS and maximum errors, the symmetric timing scheme results in higher accuracy for a fixed track duration.

The errors of the symmetric timing scheme are further scaled and compared in Figure 17. For the RMS error, the error of all three methods nicely follow the power law trend. The 2^{nd} order polynomial has a trend of $e_r \approx (dt1^*)^{1.49}$, while the other two have $e_r \approx (dt1^*)^{1.80}$. For the maximum errors, the markers deviate a little from the trend lines. In general, the 2^{nd} order polynomial is still worse than the other two methods at small $dt1^*$ but becomes comparable as $dt1^*$ increases.

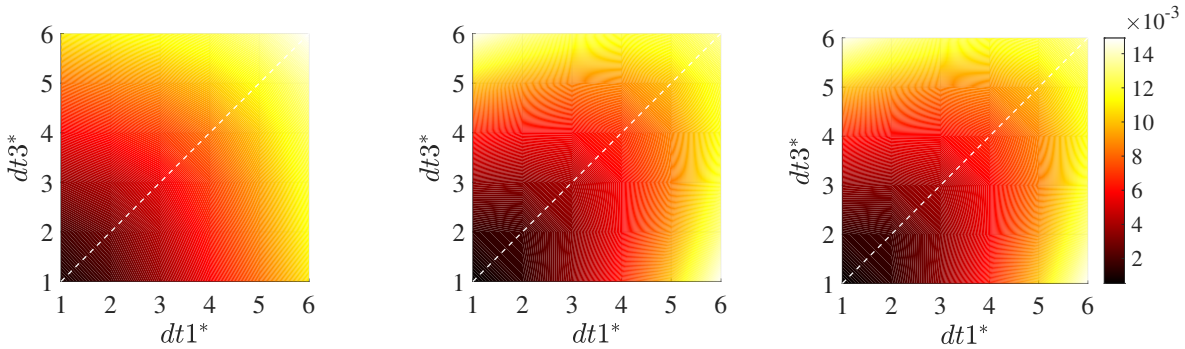

(a) 2^{nd} order polynomial **(b) 3^{rd} order polynomial** **(c) RBF-QR**

Fig. 15 Contour of e_r for different $dt1^*$ and $dt3^*$ combinations for the channel flow DNS. Dashed line indicates the symmetric timing scheme.

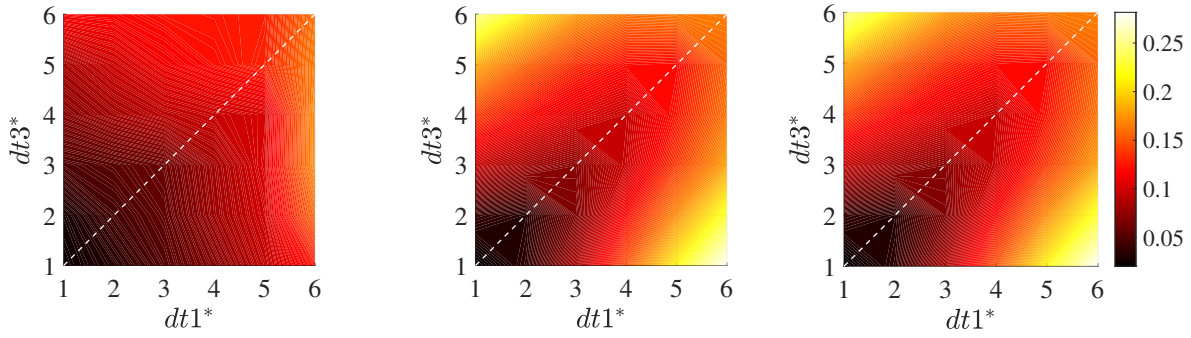

(a) 2^{nd} order polynomial **(b) 3^{rd} order polynomial** **(c) RBF-QR**

Fig. 16 Contour of $e_{r_{max}}$ for different $dt1^*$ and $dt3^*$ combinations for the channel flow DNS. Dashed line indicates the symmetric timing scheme.

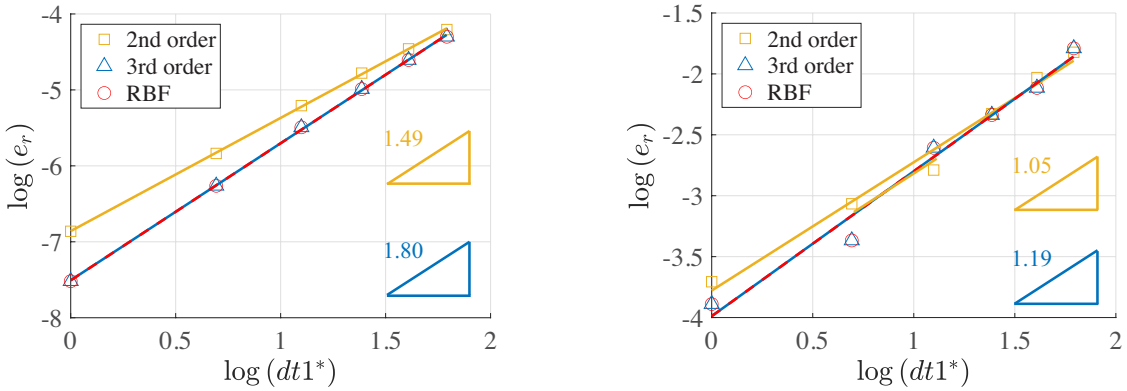

(a) e_r power scaling **(b) $e_{r_{max}}$ power scaling**

Fig. 17 Power scaling relationships for RMS and maximum errors for symmetric timing schemes for the channel flow DNS. The power factors are given in the plots.

IV. Conclusions and future work

This study assesses the effects of timing schemes on the reconstruction of pathlines using three different methods in simulated MP-STB measurements. The pathlines are determined by the particle locations at 4 time instances, which correspond to the 4 laser-pulse instances. The time between the center two pulses is constrained by the small $dt2$ PIV requirement; therefore, it is not treated as a variable in the current study. The $dt1$ and $dt3$ are thus normalized by $dt2$, and both symmetric and asymmetric timing schemes are evaluated. In general, a shorter total time duration ($dt1 + dt2 + dt3$) results in higher accuracy in the pathline reconstruction regardless of the methods as expected. For the flow fields tested in the current study, i.e., Stokes's oscillating plate, synthetic jet, and channel flow, the 2^{nd} order polynomial appears to be the worst fitting method for most timing strategies in terms of the RMS and maximum errors, while the 3^{rd} order polynomial and RBF-QR methods are comparable. Among the timing strategy combinations, the symmetric timing scheme is consistently better than an asymmetric timing scheme for a fixed total track duration. Therefore, a symmetric timing scheme is recommended in the real MP-STB experiments. In addition, the RMS errors appear to have a power law trend with $dt1^*$ for all test cases and all fitting methods. The maximum errors generally follow a power law trend; however, the maximum errors deviate a little from the trend line in the case of turbulent channel flow.

It should be noted that there are uncertainties associated with the measurements in the real MP-STB measurements, which are not considered in the current study. The optimal timing strategy corresponds to the shorted total track duration. However, proper assessment of uncertainty may allow for longer track durations with acceptable uncertainty. The

current results indicate that the errors will be flow and Reynolds number dependent, so a careful assessment of the particle location uncertainty and its propagation through subsequent calculations is required for future work.

Acknowledgments

This research was supported by a grant (Grant Number: N00014-21-1-2454) from the Office of Naval Research (ONR), monitored by Dr. David Gonzalez.

References

[1] Elsinga, G. E., Scarano, F., Wieneke, B., and van Oudheusden, B. W., "Tomographic particle image velocimetry," *Experiments in Fluids*, Vol. 41, 2006, pp. 933–947. https://doi.org/10.1007/s00348-006-0212-z.

[2] Arroyo, M. P., and Greated, C. A., "Stereoscopic particle image velocimetry," *Measurement Science and Technology*, Vol. 2, No. 12, 1991, pp. 1181–1186. https://doi.org/10.1088/0957-0233/2/12/012.

[3] Lynch, K., and Scarano, F., "A high-order time-accurate interrogation method for time-resolved PIV," *Measurement Science and Technology*, Vol. 24, No. 3, 2013.

[4] Lynch, K. P., and Scarano, F., "An efficient and accurate approach to MTE-MART for time-resolved tomographic PIV," *Experiments in Fluids*, Vol. 56, No. 66, 2015. https://doi.org/10.1007/s00348-015-1934-6.

[5] Schanz, D., Gesemann, S., and Schröder, A., "Shake-The-Box: Lagrangian particle tracking at high particle image densities," *Experiments in Fluids*, Vol. 57, No. 70, 2016. https://doi.org/10.1007/s00348-016-2157-1.

[6] Wieneke, B., "Iterative reconstruction of volumetric particle distribution," *Meas. Sci. Technol.*, Vol. 24, No. 2, 2012. https://doi.org/10.1088/0957-0233/24/2/024008.

[7] Novara, M., Schanz, D., Geisler, R., Gesemann, S., Voss, C., and Schröder, A., "Multi-exposed recordings for 3D Lagrangian particle tracking with Mutli-Pusle Shake-the-Box," *Experiments in Fluids*, Vol. 60, No. 44, 2019. https://doi.org/10.1007/s00348-019-2692-7.

[8] Janke, T., and Michaelis, D., "Uncertainty Quantification for PTV/LPT data and Adaptive Track Filtering," *14th International Symposium on Particle Image Velocimetry - ISPIV 2021*, Chicago, IL, USA, 2021.

[9] Sellappan, P., Alvi, F. S., and Cattafesta, L. N., "Lagrangian and Eulerian measurments in high-speed jets using Mutli-Pulse Shake-The-Box and fine scale reconstruction (VIC#)," *Experiments in Fluids*, Vol. 61, No. 157, 2020. https://doi.org/10.1007/s00348-020-02993-9.

[10] Novara, M., Schanz, D., Reuther, N., Kahler, C. J., and Schroder, A., "Lagrangian 3D particle tracking in high-speed flows: Shake-The-Box for multi-pulse systems," *Experiments in Fluids*, Vol. 57, No. 128, 2016. https://doi.org/10.1007/s00348-016-2216-7.

[11] Geisler, R., Novara, M., and Schroder, A., "Volumetric Multi-Pulse Particle Tracking Measurement for Separated Laminar Transitional Flow Investigations," *18th International Symposium on the Application of Laser and Imaging Techniques to Fluid Mechanics*, DLR, Lisbon, Portugal, 2016.

[12] Fornberg, B., Larsson, E., and Flyer, N., "Stable computations with Gaussian radial basis functions," *SIAM Journal on Scientific Computing*, Vol. 33, No. 2, 2011, pp. 869–892.

[13] Larsson, E., Lehto, E., Heryudono, A., and Fornberg, B., "Stable computation of differentiation matrices and scattered node stencils based on Gaussian radial basis functions," *SIAM Journal on Scientific Computing*, Vol. 35, No. 4, 2013, pp. A2096–A2119.

[14] Wright, G. B., and Fornberg, B., "Stable computations with flat radial basis functions using vector-valued rational approximations," *Journal of Computational Physics*, Vol. 331, 2017, pp. 137–156.

[15] Larsson, E., Shcherbakov, V., and Heryudono, A., "A least squares radial basis function partition of unity method for solving PDEs," *SIAM Journal on Scientific Computing*, Vol. 39, No. 6, 2017, pp. A2538–A2563.

[16] Mahesh, K., Constatinescu, G., and Moin, P., "A Numerical Method for Large-Eddy Simulation in Complex Geometries," *Journal of Computational Physics*, Vol. 197, No. 1, 2004, pp. 215–240.

[17] Babu, P. C., and Mahesh, K., "Upstream entrainment in numerical simulations of spatially evolving round jets," *Physics of Fluids*, Vol. 16, No. 10, 2004, pp. 3699–3705. https://doi.org/10.1063/1.1780548.

[18] Muppudi, S., and Mahesh, K., "Study of trajectories of jets in crossflow using direct numerical simulations," *Journal of Fluid Mechanics*, Vol. 530, 2005, pp. 81–100. https://doi.org/10.1017/S0022112005003514.

[19] Sau, R., and Mahesh, K., "Optimization of pulsed jets in crossflow," *Journal of Fluid Mechanics*, Vol. 653, 2010, pp. 365–390. https://doi.org/10.1017/S0022112010000388.

[20] Iyer, P., and Mahesh, K., "A numerical study of shear layer characteristics of low-speed transverse jets," *Journal of Fluid Mechanics*, Vol. 790, 2016, pp. 275–307. https://doi.org/10.1017/jfm.2016.7.

[21] Graham, J., Lee, M., Malaya, N., Moser, R., Eyink, G., and Meneveau, C., "Turbulent Channel Flow Data Set," Tech. rep., Johns Hopkins University, http://turbulence.pha.jhu.edu/docs/README-CHANNEL.pdf, 2014.